Materials Science & Engineering A 793 (2020) 139979

Contents lists available at ScienceDirect

Materials Science & Engineering A

journal homepage: http://www.elsevier.com/locate/msea

# Achieving equal strength joint to parent metal in a friction stir welded ultra-high strength quenching and partitioning steel

Z.W. Wang [a,b], H. Zhang [a], X.H. An [c], L.H. Wu [a], P. Xue [a,*], Q.C. Zhang [d], D.R. Ni [a], B.L. Xiao [a], Z. Y. Ma [a,**]

[a] Shenyang National Laboratory for Materials Science, Institute of Metal Research, Chinese Academy of Sciences, 72 Wenhua Road, Shenyang, 110016, China
[b] School of Materials Science and Engineering, University of Science and Technology of China, 72 Wenhua Road, Shenyang, 110016, China
[c] School of Aerospace, Mechanical and Mechatronic Engineering, The University of Sydney, Sydney, NSW, 2006, Australia
[d] CAS Key Laboratory of Mechanical Behavior and Design of Materials, University of Science and Technology of China, 443 Huangshan Road, Hefei, 230027, China

ARTICLE INFO

*Keywords:*
Equal strength joint
Ultra-high strength steel
Friction stir welding
Microstructure
Mechanical properties

ABSTRACT

The weldability of an advanced ultra-high strength quenching and partitioning (Q&P) steel with gigapascale yield strength was investigated via friction stir welding technique. The equal strength to parent metal was for the first time achieved in the friction stir welded joint although microhardness loss in heat affected zone (HAZ) occurred. The increased volume fraction of ferrite and dissolution of martensite and retained austenite were found in the softened HAZ. Nevertheless, the strength of the welded joint was unchanged due to the enhanced strain hardening ability achieved by the formation of ultra-fine dual phase structures and nano-carbide particles in the HAZ.

## 1. Introduction

With the imperative demand for light weight-high strength materials in automotive industry, the investigations of automotive steels have been evolved from conventional high strength low alloy (HSLA) steels to the third generation of advanced high strength steels (AHSSs) [1]. The main design ideas of developing the third generation steels are to significantly enhance the plasticity compared to the first generation ones and to largely reduce the manufacturing cost in comparison to the second generation ones [2].

As one of the third generation steels, quenching and partitioning (Q&P) steels were developed based on the Q&P heat-treatment process that can produce martensite based steels with retained austenite [3,4]. Benefiting from the transformation-induced plasticity (TRIP) effect during the deformation of retained austenite, the total elongation of Q&P steels can exceed 15% together with an ultra-high ultimate tensile strength (UTS) over 1000 MPa, which can be called advanced ultra-high strength steels (AUHSSs) [5,6].

As well known, welding is an indispensable procedure during the manufacture of the body-in-white in the automotive industry. However, although various welding methods have been applied to join AUHSSs [7–10], equal strength joints to parent metal (PM) are hard to achieve. This difficulty can be attributed to the unavoidable softening behavior of heat affected zone (HAZ) in steels containing martensite, which originated from the tempering and annealing softening effects during the welding thermal cycle [11–16]. The occurrence of early local deformation in the softened HAZ would result in the weakened mechanical properties and reduced joint efficiency (JE, UTS ratio of the welded joint to PM) [7,15–17].

Unlikely, the martensite in Q&P treated AUHSSs has been tempered after partitioning at certain holding temperatures [18,19], which may limit the tempering softening during the subsequent welding process. So far, the welding behaviors of Q&P 980 steels have been investigated using the fiber laser welding (LW) and the resistant spot welding (RSW), both of which showed ameliorative softening compared with other steels with similar strength [20–22]. However, the undesirable liquation defects and coarse solidification structure formed in the weld zone deteriorated the mechanical performance of the joints [21,22].

As a kind of advanced solid-state welding technique with relatively low heat input, friction stir welding (FSW) is attractive to join high melting point materials such as steels, titanium alloys and high entropy alloys [23–27], enabling the formation of the uniform and ultra-fine

* Corresponding author.
** Corresponding author.
*E-mail addresses:* pxue@imr.ac.cn (P. Xue), zyma@imr.ac.cn (Z.Y. Ma).

https://doi.org/10.1016/j.msea.2020.139979
Received 15 April 2020; Received in revised form 10 July 2020; Accepted 20 July 2020
Available online 24 July 2020

weld microstructures [28–30]. Lin et al. [31] validated the feasibility of FSW on an entry-level AUHSS, Q&P 980 steel. Full strength joints to the PM were obtained and all the joints fractured in the PM region during tensile tests, which was due to the small width and slight hardness decrease of the HAZ. Thus, high-quality joints with enhanced tensile properties are expected to achieve in AUHSSs by FSW.

In this study, a new ultra-high strength Q&P steel with gigapascale yield strength was chosen as the target material. The effect of the welding heat on the change of the microstructure and mechanical properties of the Q&P steel was investigated. The objective is to examine the weldability of the target material by FSW, explore if equal strength joint to the PM can be achieved for the ultra-high strength steels, and clarify the welding mechanism based on understanding the relationship between microstructural evolution and mechanical properties of the joint.

## 2. Experimental procedure

The commercial Q&P 1180 steel sheets with a thickness of 1.6 mm and chemical composition of Fe-0.19C-2.76Mn-1.60Si-0.039Al-0.01P-0.003S (wt%) were used. The $A_{c1}$ and $A_{c3}$ phase transformation temperatures of this steel are 746 °C and 847 °C, respectively [32]. For the FSW process, a bead-on-plate configuration was conducted to eliminate the impact of butting surface on the joint failure behavior [33]. A W-25Re alloy tool with a concave shoulder 11 mm in diameter was used. A rotation rate of 450 rpm and a welding speed of 200 mm/min were adopted. After FSW, microstructural features were systematically characterized by optical microscope (OM, Leica DMi8M), scanning electron microscope (SEM, Zeiss Supra 55) equipped with an electron backscatter diffraction (EBSD, Channel 5 software) module and transmission electron microscope (TEM, FEI Tecnai F20) combined with energy dispersive spectroscopy (EDS). The OM and SEM samples were finely ground, polished, and corroded with 5% Nital. Electrolytic polishing and twin-jet thinning were applied to prepare the EBSD and TEM specimens respectively using 10% $HClO_4$ and 90% $CH_3COOH$ solution. The step size used for EBSD mapping were 0.2 μm.

Vickers microhardness across the FSW joint was measured using a Leco LM-247AT type tester with an applied load of 200 g maintained for 15 s. Tensile specimens of the FSW joints were taken perpendicular to the welding direction according to ASTM E8/E8M-13a standard [34] with a gauge section 40 mm in length and 6 mm in width. All of the specimens were stretched by Instron 8801 testing machine at an initial strain rate of $1 \times 10^{-3}$ $s^{-1}$. A non-standard tensile specimen of 5 mm gauge length, 1.5 mm gauge width and 0.8 mm gauge thickness was machined from the HAZ parallel to the welding direction. Digital image correlation (DIC) technique with two high-speed cameras was employed to quantify the local strain evolution on the cross-section of the joint during tensile tests with an acquisition frequency of 5 images per second.

## 3. Results and discussion

### 3.1. Microstructural evolution

The temperature history during the welding process was recorded by K type thermocouple whose tip was set at the bottom of the weld center. The temperature curve illustrates that the peak temperature in the weld center reached $A_{c3}$ (Fig. S1(a)). As shown in Fig. S1(b)–(d), typical stir zone (SZ) was found under the shoulder of stir tool and the defect-free FSW joint was obtained; the sub-region of HAZ which experienced $A_{c3}$–$A_{c1}$ temperature is referred as inter-critical HAZ (IC-HAZ), and the sub-region that formed below $A_{c1}$ temperature is referred as sub-critical HAZ (SC-HAZ). These two sub-regions were also identified in the FSW of martensite + ferrite dual phase (DP) steel [35].

The microstructures of the above zones were carefully characterized. Based on the SEM, EBSD and TEM images (Fig. 1(a)–(c) and Fig. 2(a)), the PM presented multi-phase ultra-fine structures including ferrite (F), retained austenite (RA, fcc structure with red color in Fig. 1(b)) and martensite (M). The inverse pole figure (IPF) map of Fig. 1(c) reveals that there was no preferential texture. As shown in Fig. 2(a), carbides were seldom observed in the PM since the alloy elements Si and Al played crucial roles in suppressing the formation of precipitates [3,36].

As shown in Fig. 1(d), a single phase structure of martensite was observed in the SZ since austenite to martensite transformation occurred via cooling from austenite single phase field. The EBSD phase map of Fig. 1(e) indicates that barely any austenite was retained after the FSW process and no obvious change in the grain size was detected in the SZ compared to the PM. The low angle grain boundaries (LAGBs), which possessed misorientation angles below 15°, were colored in white in the EBSD IPF map of Fig. 1(f). It was clear that there is amounts of LAGBs in the SZ, suggesting that high-density substructures formed in the SZ. Correspondingly, high-density dislocation within lath martensite was observed in the TEM image of this region (Fig. 2(b)).

For the IC-HAZ, phase transformation occurred and ultra-fine DP structures with irregular shaped ferrite and martensite were found (Fig. 1(g)). As shown in Fig. 1(h), almost no austenite was observed in this region. Similar to the PM, the crystallographic orientations of these structures were relatively random, and they retained the heterogeneous morphology (Fig. 1(i)). Based on the TEM characterizations as shown in Fig. 2(c) and (d), martensite laths with widths of 100–300 nm were formed. One notable phenomenon was that the volume fraction of the ferrite was increased apparently in this region compared to the PM.

In comparison to the IC-HAZ, the volume fraction and the grain size of the austenite in the SC-HAZ were similar (Fig. 1(j)–(l)). Additionally, the phase transformation from ferrite to austenite did not occur and the tempering of martensite proceeded in the SC-HAZ with a number of carbide particles precipitating along grain boundaries (Figs. 1(j) and 2(e)). Fig. 2(f) shows the typical conglobate or short rod-like carbide particles ($M_3C$) with diameters less than 50 nm. According to the EDS maps in Fig. 2(f), these particles were Mn-rich carbides, which was consistent with the previous work [37]. As well known, the addition of Si would increase the nucleation rate and reduce the growth rate of carbides, and the addition of Mn would slow down the aggregation and spheroidization of carbides in steels [38]. So, both of them contribute to the formation of nano-carbide particles in the SC-HAZ.

### 3.2. Mechanical properties

The microhardness profiles measured in the cross-sectional plane are illustrated in Fig. 3(a). There is an apparent hardness drop of near 80 Hv in softened HAZ when compared to that of the PM (375 Hv). It should be noted that the minimum microhardness value was detected in the SC-HAZ next to the IC-HAZ. In the IC-HAZ, the variation of volume fraction of the ferrite phase played a key role in the material softening. As shown in Fig. S1(b), when the peak temperature was located at the range of $Ac_1$ to $Ac_3$, the soft phase of ferrite formed, resulting in the loss of microhardness. Actually, the volume fraction of the ferrite gradually increased away from the SZ (Fig. S2), which can be predicted according to the Fe–$Fe_3C$ phase diagram in Fig. S1(b).

Tempering induced softening of martensite, which was well accepted in the welding of steels [7,12,15,20,26,39], was considered firstly for the hardness decrease in the SC-HAZ. The precipitation of the carbide particles during the dissolution of the martensite validated the proceeding of martensite tempering during the welding thermal cycle (Figs. 1(j) and 2(f)). Except for the tempering induced softening of martensite, the dissolution of retained austenite could also result in the hardness drop in the SC-HAZ, as proposed by Mironov et al. [9] in the FSW of ultra-high strength TRIP steel. The retained austenite was believed to be harder than ferrite and/or bainite due to relatively higher carbon content. In the present work, the volume fraction of retained austenite was estimated to be at least 2.54% in the PM based on the EBSD results. However, most of them dissolved and transformed into

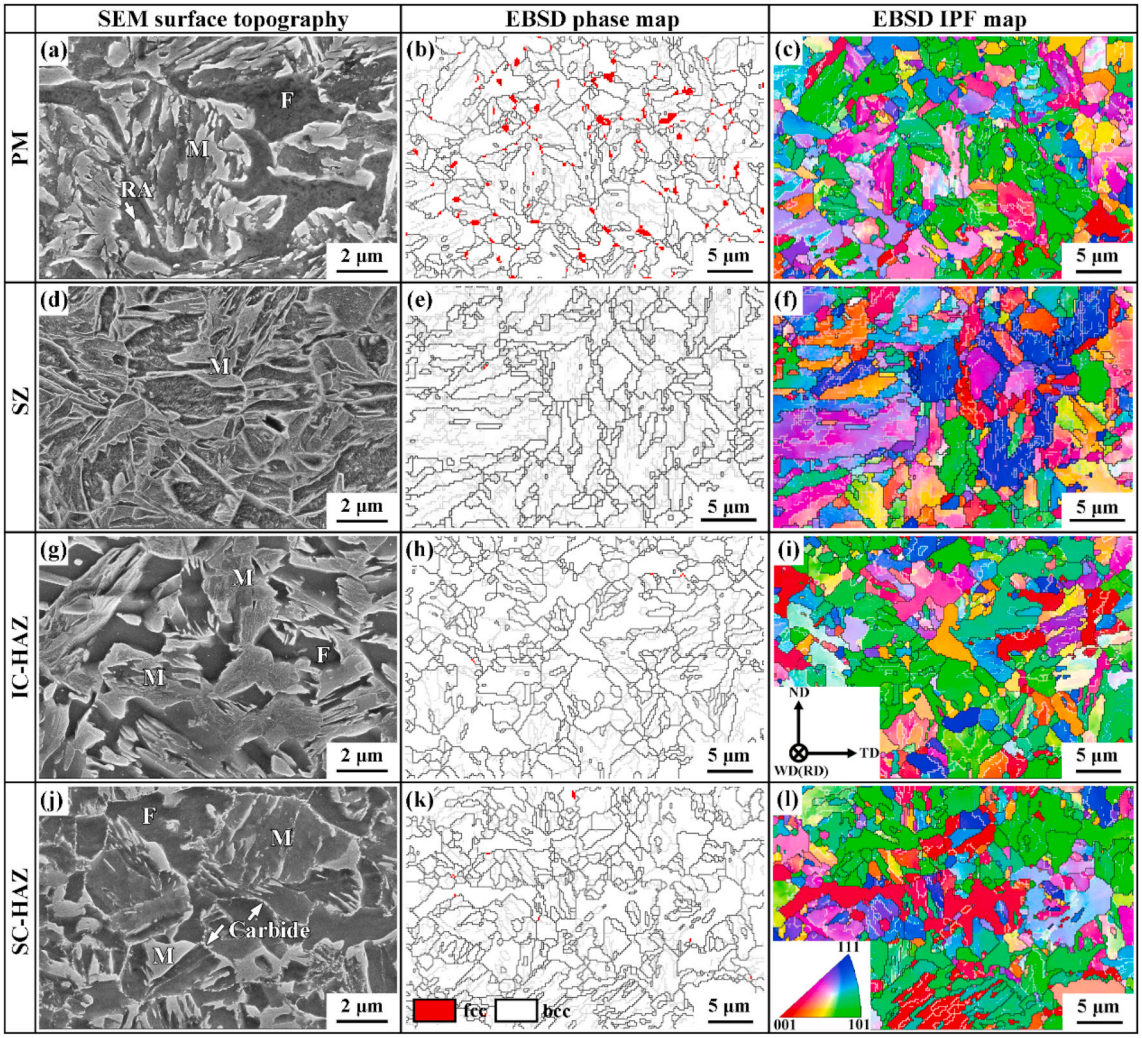


**Fig. 1.** SEM images of PM, SZ, IC-HAZ and SC-HAZ.

ferrite and carbides due to the heating effect induced by FSW (Fig. 1(j) and (k)). Therefore, the loss of strengthening effects of both the martensite and retained austenite could be the main softening mechanism in the SC-HAZ.

The microhardness profiles illustrated that the SZ exhibited the highest hardness of ~480 Hv (Fig. 3(a)). As revealed in Fig. 1(d)–(f) and Fig. 2(b), the hardness enhancement in the SZ was strongly associated with the generation of the dislocation martensite which possessed high hardness and strength in steels. As shown in Fig. 3(b), the PM possessed the yield strength (YS) and UTS of 1048 MPa and 1214 MPa, respectively. By comparison, the YS and UTS of the welded joint were 1028 and 1212 MPa, respectively, indicating that the joint with significantly softened HAZ showed equal strength to the PM (JE ~ 100%), which was rarely achieved in ultra-high strength steels before [7–9,39]. Also, the welded specimen exhibited comparable ductility and fractured in the PM rather than the HAZ, as revealed in the inset of Fig. 3(b). However, owing to the non-uniform properties of the different zones across the joint, local deformation proceeded in the HAZ and the PM during the tensile test (see DIC results in Section 3.3 for details), leading to less elongation of the welded joint compared to the PM.

### 3.3. Strengthening mechanism

To understand why the strength of the joint with softened HAZ was impervious, the evolution of local strains during tensile tests in the areas of PM, HAZ and SZ was obtained using the DIC technique. As shown in Fig. 4(a), five representative deformation stages, divided into elastic deformation (total strain = 0.4%), $\sigma_{0.2}$ yield point (total strain = 0.76%), interim plastic deformation (total strain = 5%), maximum loading point (total strain = 9.3%) and localized necking (total strain = 11%), were selected to exhibit the corresponding local strain distribution in the cross-sectional plane of the FSW joint (Fig. 4(c)). At the early stages of deformation (elastic deformation and $\sigma_{0.2}$ yield stages), apparent strain concentration was found in the HAZ due to the lowest hardness, indicating that this region suffered larger deformation compared to the PM and SZ. In addition, the local strain was more intensive on the bottom of the weld seam, which could be attributed to the larger HAZ width near the weld bottom as shown in Fig. 3(a).

In the interim plastic deformation stage, the HAZ and PM undertook much larger local deformation compared to the SZ, reflected by the local axial strain profile in Fig. 4(b). In particular, the axial strain in the HAZ was mainly concentrated in the SC-HAZ, which was consistent with the location of the minimum hardness zone in Fig. 3(a). The local strain profile was almost symmetrical relative to the weld center and similar peak strain could be detected in the HAZ and PM. This case was associated with the excellent work hardening capability of the HAZ due to the tempering. At the maximum loading and the localized necking stages, local deformation was significantly prominent in the PM.

Based on the evolution of local strains, it was suggested that softened microstructures in the HAZ possessed almost the same even superior

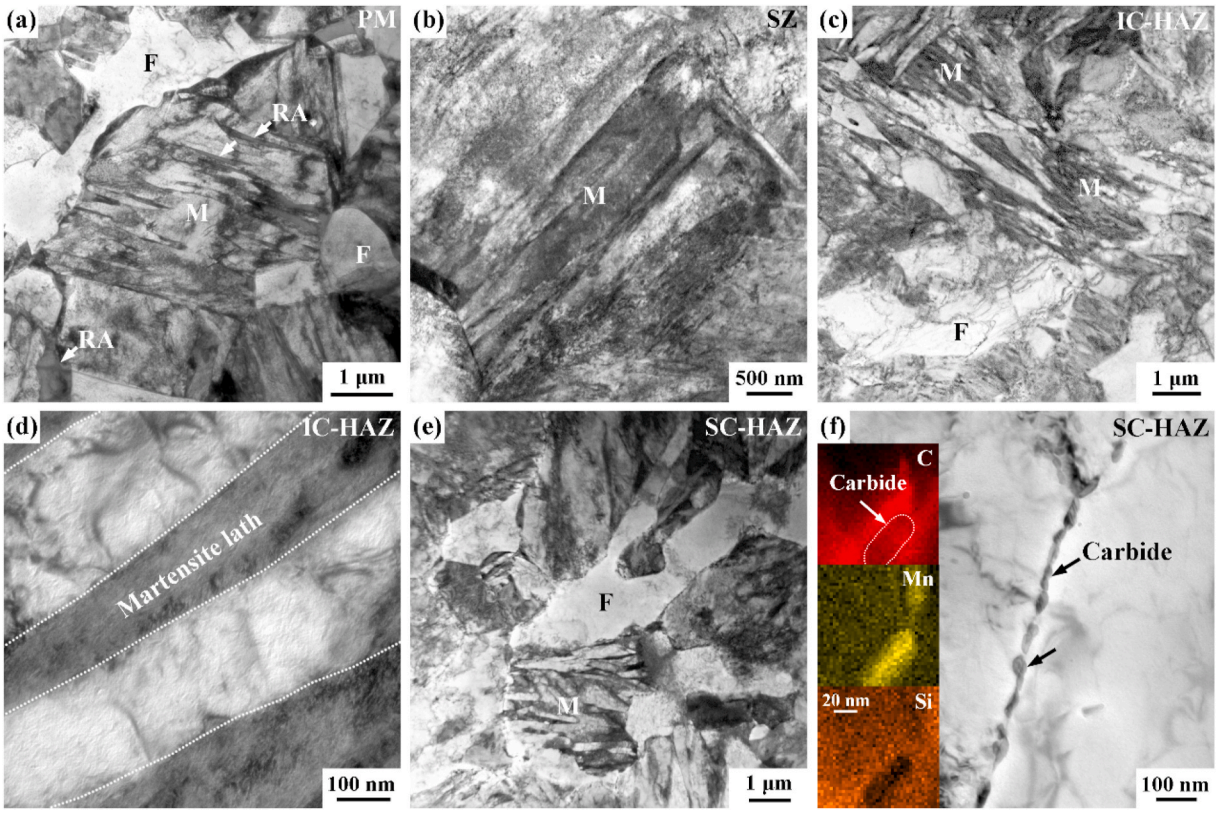


**Fig. 2.** TEM images of the joint. (a) PM, (b) SZ, (c) and (d) IC-HAZ, (e) and (f) SC-HAZ. The insets of (f) are the EDS mappings around carbide.

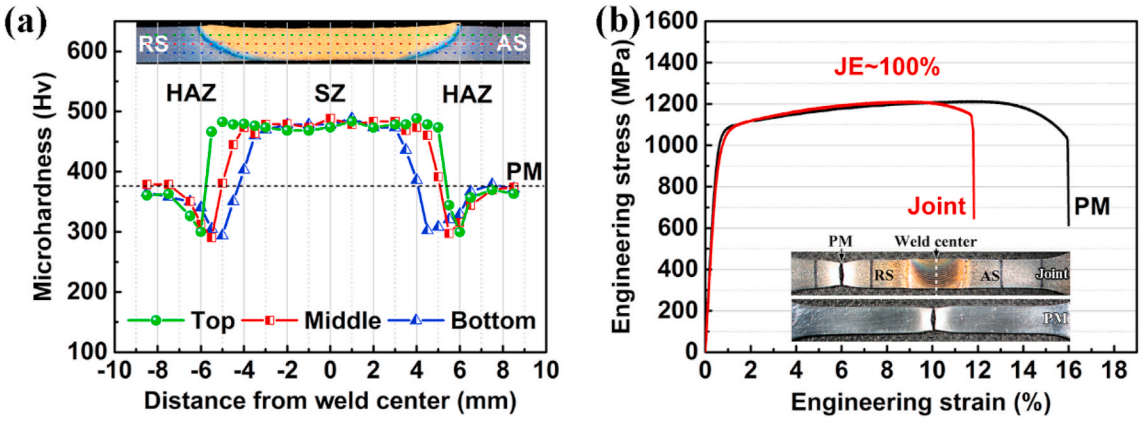


**Fig. 3.** (a) Cross-sectional microhardness profiles of FSW joint, and (b) engineering stress-strain curves of FSW joint and the PM (AS and RS mean the advancing and retreating side, respectively).

strain hardening ability compared with that of the PM, which can be verified by the obvious hardness recovery of the HAZ after tensile test, as shown in Fig. S3(a). In addition, the tensile curves showed in Fig. S3(b) indicated that the HAZ possessed a higher initial strain hardening rate and lower yield strength in comparison to the PM, which was corresponding with the higher strength and lower hardness of the joint, respectively.

The superior strain hardening ability of the HAZ could be expounded as follows. At the early stage of deformation, the ferrites and tempered martensite that were formed in the two sub-regions of the HAZ played crucial roles in accommodating the local strain and then the accumulations of dislocations could make significant contributions to the work hardening. With the deformation continuing, the nano-carbide particles might significantly contribute to enhancing the work hardening by pinning and trapping the dislocations during plastic deformation. Finally, the plastic instability happened in the PM, leading to the occurrence of the failure in the PM rather than in the HAZ.

## 4. Conclusions

The friction stir welded Q&P 1180 steel joint exhibited equal strength to the PM even though there was an apparent hardness drop in the HAZ. The softening of the HAZ was attributed to the increase of ferrite content and dissolution of martensite and retained austenite. Nevertheless, the generation of ultra-fine DP structures and the formation of nano-carbide particles were suggested to enhance the strain hardening ability of the HAZ, which resulted in the excellent joint strength during subsequent tensile deformation. The welded joint

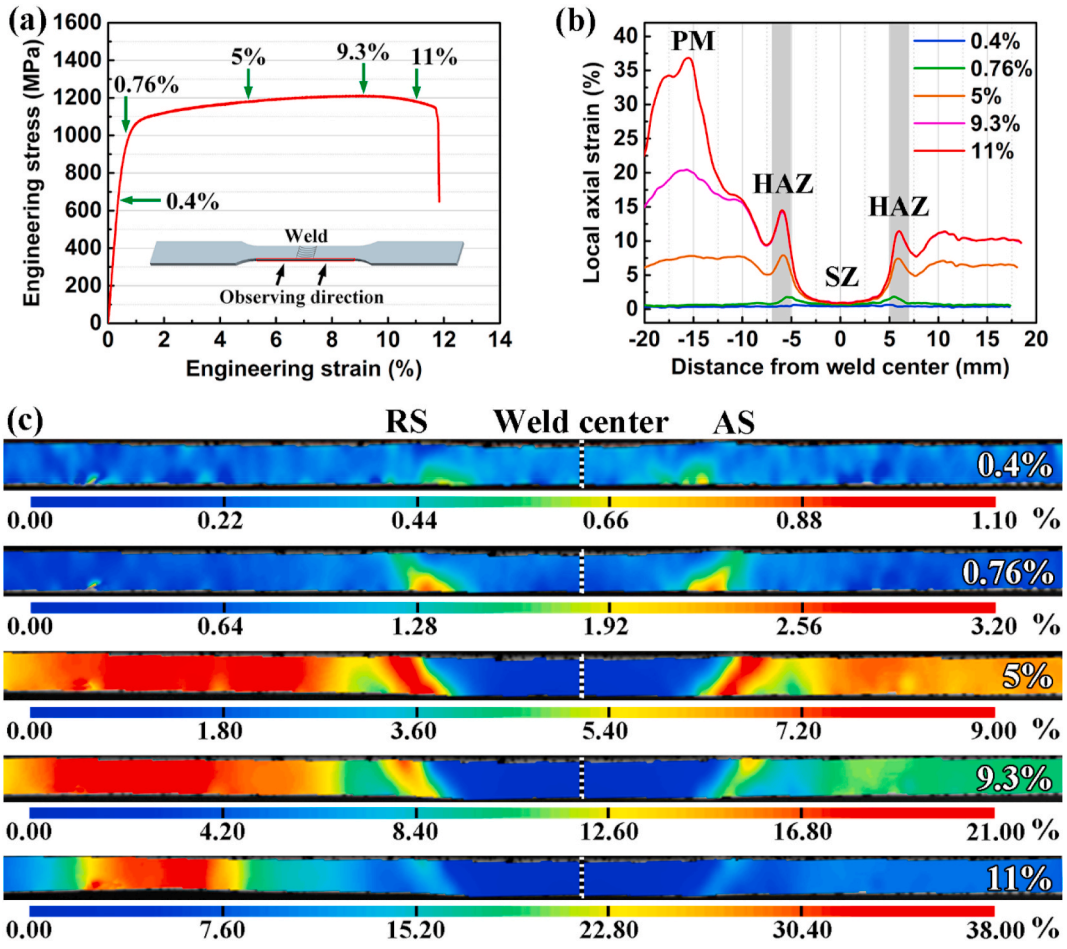


**Fig. 4.** DIC test results of joint. (a) Stress-strain curve marked with five concerned global strain stages, (b) local axial strain profiles at the corresponding strain stages in (a), (c) local strain distributions in the weld cross-section at the corresponding strain stages in (a).

owned less elongation than the PM due to the proceeding of the local deformation in the HAZ and the PM region. This work provides an effective strategy to improve the welding quality of the ultra-high strength steel.

## Data availability

The raw/processed data required to reproduce these findings cannot be shared at this time as the data also forms part of an ongoing study.

## Declaration of competing interest

The authors declare that they have no known competing financial interests or personal relationships that could have appeared to influence the work reported in this paper.

## CRediT authorship contribution statement

**Z.W. Wang:** Investigation, Data curation, Writing - original draft. **H. Zhang:** Methodology, Software. **X.H. An:** Conceptualization, Writing - review & editing. **L.H. Wu:** Methodology, Formal analysis. **P. Xue:** Formal analysis, Supervision, Funding acquisition, Writing - review & editing. **Q.C. Zhang:** Methodology, Software. **D.R. Ni:** Methodology, Formal analysis. **B.L. Xiao:** Methodology, Formal analysis. **Z.Y. Ma:** Supervision, Writing - review & editing.

## Acknowledgements

This work was supported by the National Natural Science Foundation of China under Grant Nos. 51671190 and 51901225, and the Youth Innovation Promotion Association of the Chinese Academy of Sciences (2017236). X.H. An acknowledges the financial support from Australia Research Council (DE170100053) and the Robinson Fellowship Scheme of the University of Sydney (G200726).

## Appendix A. Supplementary data

Supplementary data to this article can be found online at https://doi.org/10.1016/j.msea.2020.139979.

## References

[1] J.H. Schmitt, T. Iung, New developments of advanced high-strength steels for automotive applications, C. R. Phys. 19 (2018) 641–656.
[2] J.W. Zhao, Z.Y. Jiang, Thermomechanical processing of advanced high strength steels, Prog. Mater. Sci. 94 (2018) 174–242.
[3] J. Speer, D.K. Matlock, B.C. De Cooman, J.G. Schroth, Carbon partitioning into austenite after martensite transformation, Acta Mater. 51 (2003) 2611–2622.
[4] A.J. Clarke, J.G. Speer, M.K. Miller, R.E. Hackenberg, D.V. Edmonds, D.K. Matlock, F.C. Rizzo, K.D. Clarke, E. De Moor, Carbon partitioning to austenite from martensite or bainite during the quench and partition (Q&P) process: a critical assessment, Acta Mater. 56 (2008) 16–22.
[5] J.G. Speer, E. De Moor, A.J. Clarke, Critical assessment 7: quenching and partitioning, Mater. Sci. Technol. 31 (2015) 3–9.
[6] J.G. Speer, F.C. Rizzo Assunção, D.K. Matlock, D.V. Edmonds, The "quenching and partitioning" process: background and recent progress, Mater. Res. 8 (2005) 417–423.

[7] M. Matsushita, Y. Kitani, R. Ikeda, M. Ono, H. Fujii, Y.D. Chung, Development of friction stir welding of high strength steel sheet, Sci. Technol. Weld. Join. 16 (2011) 181–187.
[8] C. Luo, Y. Cao, Y. Zhao, L. Zhao, J. Shan, Fiber laser welding of 1700-MPa, ultrahigh-strength steel, Weld. J. 97 (2018) 214–228.
[9] S. Mironov, Y.S. Sato, S. Yoneyama, H. Kokawa, H.T. Fujii, S. Hirano, Microstructure and tensile behavior of friction-stir welded TRIP steel, Mater. Sci. Eng. A 717 (2018) 26–33.
[10] F. Xing, X.M. Qiu, L. Zhao, Y. Ruan, D.F. Wang, Hardening, softening, and mechanical properties in ultra-high-strength DP1180 tailor-welded blanks, J. Mater. Eng. Perform. 28 (2019) 2086–2093.
[11] J.F. Wang, L.J. Yang, M.S. Sun, T. Liu, H. Li, A study of the softening mechanisms of laser-welded DP1000 steel butt joints, Mater. Des. 97 (2016) 118–125.
[12] Y. Hovanski, M.L. Santella, G.J. Grant, Friction stir spot welding of hot-stamped boron steel, Scr. Mater. 57 (2007) 873–876.
[13] M. Ghosh, K. Kumar, R.S. Mishra, Analysis of microstructural evolution during friction stir welding of ultrahigh-strength steel, Scr. Mater. 63 (2010) 851–854.
[14] G. Weber, H. Thommes, H. Gaul, O. Hahn, M. Rethmeier, Resistance spot welding and weldbonding of advanced high strength steels, Mat.-wiss. u. Werkstofftech. 41 (2010) 931–939.
[15] H.Y. Gong, S.F. Wang, P. Knysh, Y.P. Korkolis, Experimental investigation of the mechanical response of laser-welded dissimilar blanks from advanced- and ultra-high-strength steels, Mater. Des. 90 (2016) 1115–1123.
[16] J. Jia, S.L. Yang, W.Y. Ni, J.Y. Bai, Microstructure and mechanical properties of fiber laser welded joints of ultrahigh-strength steel 22MnB5 and dual-phase steels, J. Mater. Res. 29 (2014) 2565–2575.
[17] M. Pouranvari, S.P.H. Marashi, D.S. Safanama, Failure mode transition in AHSS resistance spot welds. Part II: experimental investigation and model validation, Mater. Sci. Eng. A 528 (2011) 8344–8352.
[18] M.J. Santofimia, L. Zhao, R. Petrov, J. Sietsma, Characterization of the microstructure obtained by the quenching and partitioning process in a low-carbon steel, Mater. Charact. 59 (2008) 1758–1764.
[19] M.J. Santofimia, R.H. Petrov, L. Zhao, J. Sietsma, Microstructural analysis of martensite constituents in quenching and partitioning steels, Mater. Charact. 92 (2014) 91–95.
[20] W. Guo, Z.D. Wan, P. Peng, Q. Jia, G.S. Zou, Y. Peng, Microstructure and mechanical properties of fiber laser welded QP980 steel, J. Mater. Process. Technol. 256 (2018) 229–238.
[21] W.D. Li, L.X. Ma, P. Peng, Q. Jia, Z.D. Wan, Y. Zhu, W. Guo, Microstructural evolution and deformation behavior of fiber laser welded QP980 steel joint, Mater. Sci. Eng. A 717 (2018) 124–133.
[22] X.D. Liu, Y.B. Xu, R.D.K. Misra, F. Peng, Y. Wang, Y.B. Du, Mechanical properties in double pulse resistance spot welding of Q&P 980 steel, J. Mater. Process. Technol. 263 (2019) 186–197.
[23] H. Zhang, D. Wang, P. Xue, L.H. Wu, D.R. Ni, B.L. Xiao, Z.Y. Ma, Achieving ultra-high strength friction stir welded joints of high nitrogen stainless steel by forced water cooling, J. Mater. Sci. Technol. 34 (2018) 2183–2188.
[24] L.H. Wu, X.B. Hu, X.X. Zhang, Y.Z. Li, Z.Y. Ma, X.L. Ma, B.L. Xiao, Fabrication of high-quality Ti joint with ultrafine grains using submerged friction stirring technology and its microstructural evolution mechanism, Acta Mater. 166 (2019) 371–385.
[25] K. Liu, S.S. Nene, M. Frank, S. Sinha, R.S. Mishra, Metastability-assisted fatigue behavior in a friction stir processed dual-phase high entropy alloy, Mater. Res. Lett. 6 (2018) 613–619.
[26] Z.W. Wang, G.N. Ma, B.H. Yu, P. Xue, G.M. Xie, H. Zhang, D.R. Ni, B.L. Xiao, Z. Y. Ma, Improving mechanical properties of friction-stir-spot-welded advanced ultra-high-strength steel with additional water cooling, Sci. Technol. Weld. Join. 25 (2020) 336–344.
[27] L.H. Wu, H. Zhang, X.H. Zeng, P. Xue, B.L. Xiao, Z.Y. Ma, Achieving superior low temperature and high strain rate superplasticity in submerged friction stir welded Ti-6AI-4V alloy, Sci. China Mater. 61 (2018) 417–423.
[28] R.S. Mishra, Z.Y. Ma, Friction stir welding and processing, Mater. Sci. Eng. R 50 (2005) 1–78.
[29] P. Xue, B.B. Wang, X.H. An, D.R. Ni, B.L. Xiao, Z.Y. Ma, Improved cyclic softening behavior of ultrafine-grained Cu with high microstructural stability, Scr. Mater. 166 (2019) 10–14.
[30] P. Xue, Z.Y. Huang, B.B. Wang, Y.Z. Tian, W.G. Wang, B.L. Xiao, Z.Y. Ma, Intrinsic high cycle fatigue behavior of ultrafine grained pure Cu with stable structure, Sci. China Mater. 59 (2016) 531–537.
[31] H.T. Lin, H.T. Jiang, Y.S. Wang, S.W. Tian, Microstructure gradient characteristics and mechanical properties of friction stir welded high strength QP980 steel, Mater. Res. Express 6 (2019) 126584.
[32] J. Trzaska, L.A. Dobrzański, Modelling of CCT diagrams for engineering and constructional steels, J. Mater. Process. Technol. 192–193 (2007) 504–510.
[33] Q. Shang, D.R. Ni, P. Xue, B.L. Xiao, Z.Y. Ma, Evolution of local texture and its effect on mechanical properties and fracture behavior of friction stir welded joint of extruded Mg-3A1-1Zn alloy, Mater. Charact. 128 (2017) 14–22.
[34] ASTM Standard E8/E8M-13a, Standard Test Methods for Tension Testing of Metallic Materials, ASTM International, West Conshohocken, PA, 2013.
[35] M. Mahmoudiniya, A.H. Kokabi, S. Kheirandish, L.A.I. Kestens, Microstructure and mechanical properties of friction stir welded ferrite-martensite DP700 steel, Mater. Sci. Eng. A 737 (2018) 213–222.
[36] D.K. Matlock, V.E. Bräutigam, J.G. Speer, Application of the quenching and partitioning (Q&P) process to a medium-carbon, high-Si microalloyed bar steel, Mater. Sci. Forum 426–423 (2003) 1089–1094.
[37] E.J. Seo, L. Cho, Y. Estrin, B.C. De Cooman, Microstructure-mechanical properties relationships for quenching and partitioning (Q&P) processed steel, Acta Mater. 113 (2016) 124–139.
[38] G. Miyamoto, J. Oh, K. Hono, T. Furuhara, T. Maki, Effect of partitioning of Mn and Si on the growth kinetics of cementite in tempered Fe–0.6 mass% C martensite, Acta Mater. 55 (2007) 5027–5038.
[39] M. Ghosh, K. Kumar, R.S. Mishra, Friction stir lap welded advanced high strength steels: microstructure and mechanical properties, Mater. Sci. Eng. A 528 (2011) 8111–8119.